6
Shielded Metal Arc Welding (SMAW) Technique

The chapter discusses the characteristics of dissimilar weld joints (DWJ) between P91 and Incoloy 800HT with a widely used shielded metal arc welding (SMAW) process. The chapter comprehends the microstructural characteristics that evolved during the welding and its effect on the mechanical properties of the joint obtained.

6.1 MACROSCOPIC OBSERVATIONS

The welded plate from the front and back sides can be observed in Figure 6.1(a-b), with clearly visible significant angular distortion. The angular distortion was measured to be 3.2˚. Figure 6.1(c) reveals the cross-section of the joint to show the weld bead and its depth of penetration. The multiple welding passes induced heavy thermal stresses, causing heavy distortion. The consequent welding passes required high welding skills as cleaning of deposited slag is crucial after each pass. Also, slag inclusion in subsequent passes is of high risk. A macro examination showed multiple welding passes without any visible flaws in the fusion zone or along the weld interfaces. The macrostructure also showed a 6 mm wide P91 heat affected zone. The obtained weld was free from any porosity, cracks, and inclusions. The HAZ was not observed with any distinct or significant changes, and the features were the same as discussed in section 5.4.2.

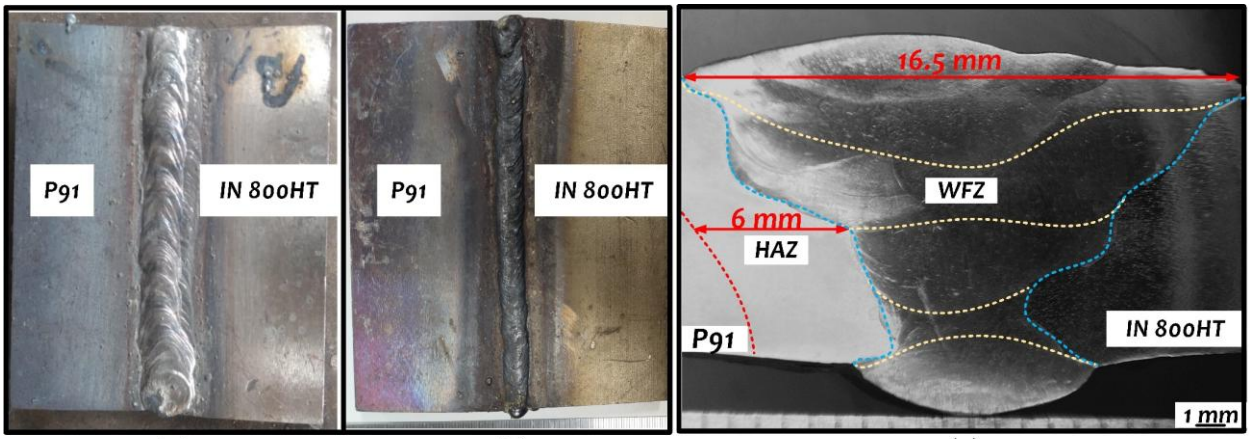


Figure 6.1 : (a) Welded plate top face (b) welded plate bottom face (c) SMAW weld macrostructure

6.2 WELD INTERFACE AND WELD FUSION ZONE (WFZ) MICROSTRUCTURE CHARACTERIZATION

The light optical microscopic images in Figure 6.26(a-f) show the AW state specimen, while Figure 6.2(g-i) shows the PWHT state specimen. Figure 6.2(a-c) displays the P91 weld interface, WFZ, and Incoloy 800HT weld interface from the top of the weld, respectively. Figure 6.2(d-f) shows the same interfaces from the center of the weld. The optical analysis of the P91 weld interface showed the presence of macrosegregation in the form of peninsulas

and islands. The Incoloy 800HT weld interface had extensive austenitic grain growth near the weld interface. Some regions of the Incoloy 800HT weld interface near the center region had the formation of a transition zone and a Type II boundary. A Type II boundary denotes a distinct grain boundary that emerges amidst columnar grains during solidification. The Incoloy 800HT weld interface near the top of the weld had thicker transition zones and an unmixed zone. In the center of the weld was columnar dendritic growth at the interface and well-extended austenitic grain boundaries. Near the weld root, a Type II boundary was formed. This variation in the interface is due to different solidification rates from multiple weld passes. The WFZ had randomly distributed columnar and equiaxed dendritic patches. SGBs, SSGBs, and MGBs were also present. The cells or dendrites exhibited distinct boundaries. This differentiation can be attributed to the redistribution of solutes, commonly referred to as the SSGB. The boundary formed by the intersection of sub-grains or cells within a similar group can be referred to as SGB. SGBs and SSGBs form as the liquid film between two grains, and dendrites solidify last, respectively. Simultaneously, a grain boundary with a high-angle misorientation, where the crystallographic component moves apart from its compositional component, can be referred to as MGB. MGBs formed due to rapid solidification in some regions of the WFZ.

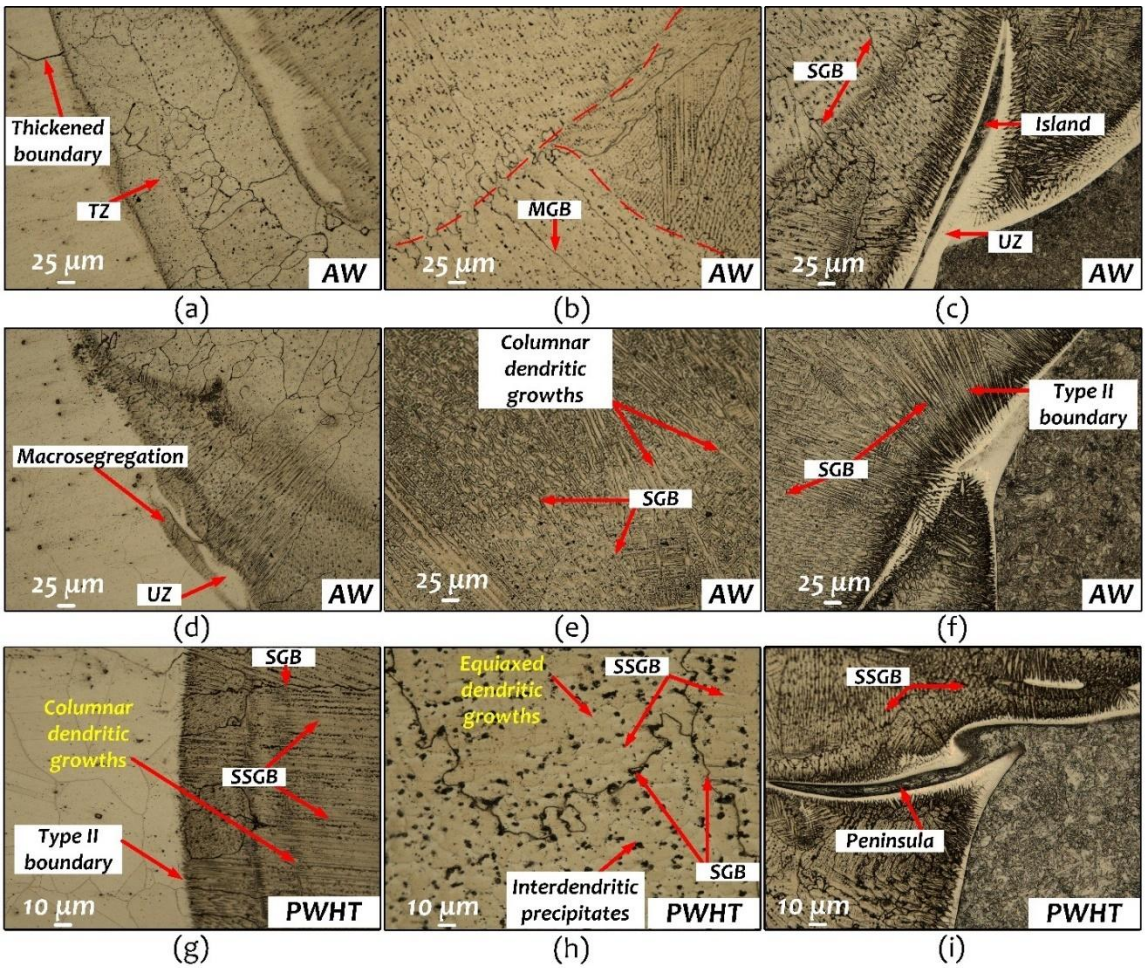


Figure 6.2 : Optical micrographs of (a) Incoloy 800HT weld interface (near weld top) (b) WFZ (near weld top) (c) P91 weld interface (near weld top) (d) Incoloy 800HT weld interface (near weld center) (e) WFZ (near weld center) (f) P91 weld interface (near weld center) (g) Incoloy 800HT weld interface (near weld root) (h) WFZ (near weld root) (i) P91 weld interface (near weld root)

Figure 6.3(a-b) shows the WFZ in AW and PWHT states. The columnar dendritic regions in AW and PWHT states were observed with SSGBs, SGB, interdendritic particles, and dendritic cores. The EDS spectrum in Figure 6.3(c) confirms the presence of C-rich

phases in the interdendritic region of the WFZ, while the interdendritic regions show Ti diffused into a liquid phase during solidification (Tan et al., 2011). Figure 6.3(d) shows high C deposition in the interdendritic region after PWHT.

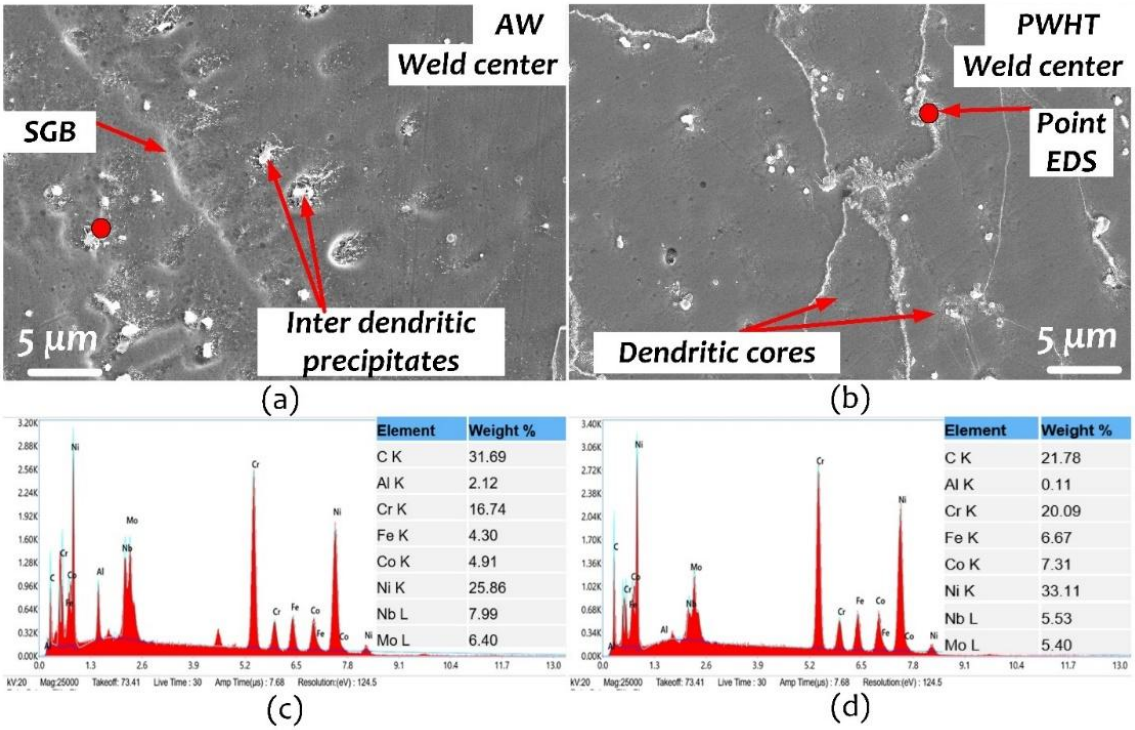


Figure 6.3 : FESEM micrograph and EDS spectrum of (a) WFZ in AW state (b) WFZ in PWHT state (c) spotted interdendritic particles in AW states WFZ (d) spotted interdendritic particles in PWHT states WFZ

The FCC crystal structure of Ni-based alloys leads to slower diffusion rates of alloying elements, causing microsegregation during welding solidification (Palanivel et al., 2021). Table 6.1 presents the elemental compositions in the dendritic core and interdendritic region. The PWHT sample was examined using EDS to measure the elemental compositions in the WFZ's dendritic cores and interdendritic regions. Segregation coefficients were calculated from the EDS data by using (equation (6.1)) (Rakoczy et al., 2020). Fe, Co, and Ni segregation coefficients were greater than 1, indicating that these elements were present in the solidified dendritic core (solid phase). The results of the EDS analysis showed that while Ni did not significantly segregate during solidification, elements such as C, Cr, Nb, and Mo were found to have segregated into the interdendritic region of the WFZ. Nb was mainly seen to concentrate in the interdendritic region. Cr segregation led to the formation of carbides, which could have had a negative impact on the material's mechanical properties. C segregation also had a negative effect. Also, the cooling and reheating during the multipass welds promote the change in composition. The segregation coefficient k, calculated as the ratio of the average element concentration of the alloying elements in the dendritic core and interdendritic region of the WFZ, determines the extent of segregation of the alloying elements.

$$\text{Segregation coefficient k} = \frac{C_S(\text{Solid})}{C_L(\text{Liquid})} \tag{6.1}$$

Table 6.1 : Segregation coefficient and elemental composition of different structures investigated in the WFZ

Spectrum	*Position*	*C*	*Cr*	*Fe*	*Co*	*Ni*	*Nb*	*Mo*
EDS (weight %)	Dendritic core (C_S)	30.67	16.93	6.23	7.45	31.90	3.01	3.81
	Interdendritic region (C_L)	32.32	17.21	5.11	7.33	30.66	3.16	4.21
	Segregation coefficient k	0.9	0.9	1.2	1.01	1.04	0.9	0.9

EPMA analysis was conducted to examine diffusion and segregation at the weld interfaces and nearby solidified WFZ regions. Figure 6.4 shows the EPMA results for the P91 weld interface. The WFZ was enriched with C, likely resulting from different carbide formations (Mo, Ti, Cr-based). Heavy carbon segregation was seen in the interdendritic region of the WFZ near the P91 weld interface. Depletion of Cr was noticed in the P91 HAZ near the weld interface, while Fe diffusion into the weld fusion zone was evident. Mo and Ni segregation near the dendritic region was also seen. Co showed no segregation activity. Figure 6.4 shows the EPMA results for the Incoloy 800HT weld interface. The C-deposited region suggests C-rich precipitates, but no heavy segregation of carbon was observed. Ti-rich precipitates were evenly distributed.

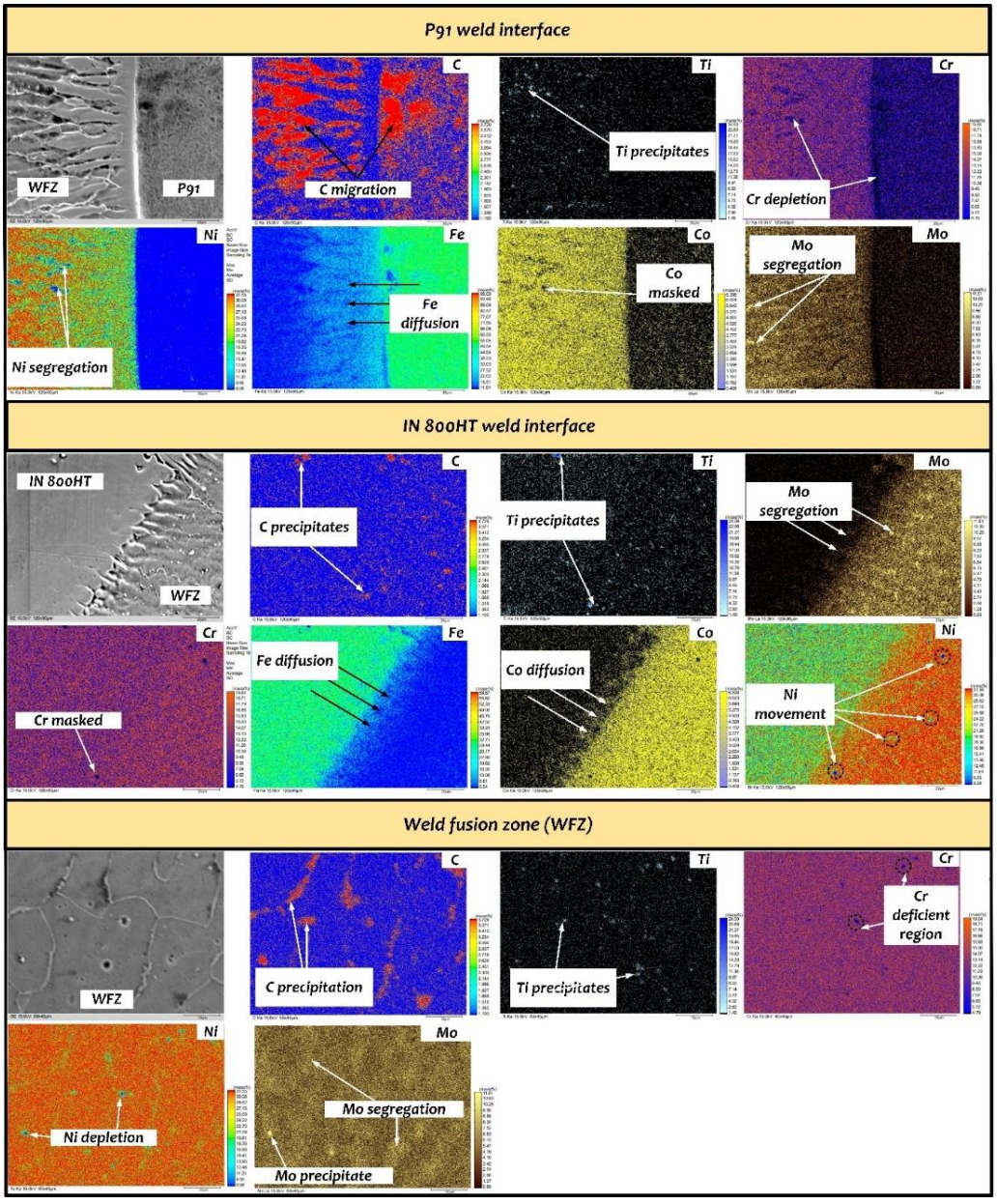


Figure 6.4 : EPMA qualitative analysis of P91 weld interface, Incoloy 800HT weld interface, and WFZ

Cr was slightly high in the WFZ near the Incoloy 800HT weld interface, and Fe concentration was higher in the WFZ due to diffusion. Ni movement was restricted near the Incoloy 800HT region since the WFZ had a higher Ni composition. Mo was found to be segregated near the columnar dendritic region in the WFZ due to the effect of multiple thermal cycles during the welding deposition. Variation in Co composition from WFZ to Incoloy 800HT HAZ was seen and may have been due to diffusion activity in the transition

zone at the weld interface while in a partially melted state. Further, the EPMA scan for WFZ in Figure 6.4 shows an evident deposition of carbon over the SGBs and a heavy presence of Ti-rich precipitates in the WFZ. Mo segregation was also witnessed in the dendritic cores, detrimental to the mechanical properties. Ni depletion was also observed over the SGBs in the WFZ.

The Electron Backscatter Diffraction (EBSD) scan (Figure 6.5) showed random orientation of the P91 HAZ grain near the P91 weld interface in the WFZ. The Inverse pole figure (IPF) map (Figure 6.5(a)) showed different orientations of the dendritic groups in the WFZ. The Kernel average misorientation (KAM) map (Figure 6.5(b)) indicated high levels of local strain in the P91 HAZ and uneven distribution in the WFZ. In the EBSD scan (Figure 6.6) for the Incoloy 800HT weld interface, the IPF map (Figure 6.6(a)) showed the random orientation of grains, and the KAM map (Figure 6.6(b)) revealed high levels of dislocations and strains in the WFZ compared to the HAZ regions. The phase maps indicated the presence of BCC crystal structure (Figure 6.5(c)) in the P91 HAZ and FCC crystal structure (Figure 6.6(c)) in the Incoloy 800HT and WFZ. The Incoloy 800HT weld interface has extensive grain growth into the WFZ, indicating epitaxial growth near the weld interface. In comparison, the P91 weld interface had a distinguished weld interface, and dendritic growth in varied orientations was observed at the weld interface. It could be inferred from the results that WFZ solidification was mostly austenitic. KAM map showed an uneven distribution of dislocations across the weld interface, which makes the WFZ and HAZ regions highly prone to failure. In a similar study by (Sakthivel et al., 2022), KAM showed higher strain distribution in the P91 HAZ region, contributing to the failure.

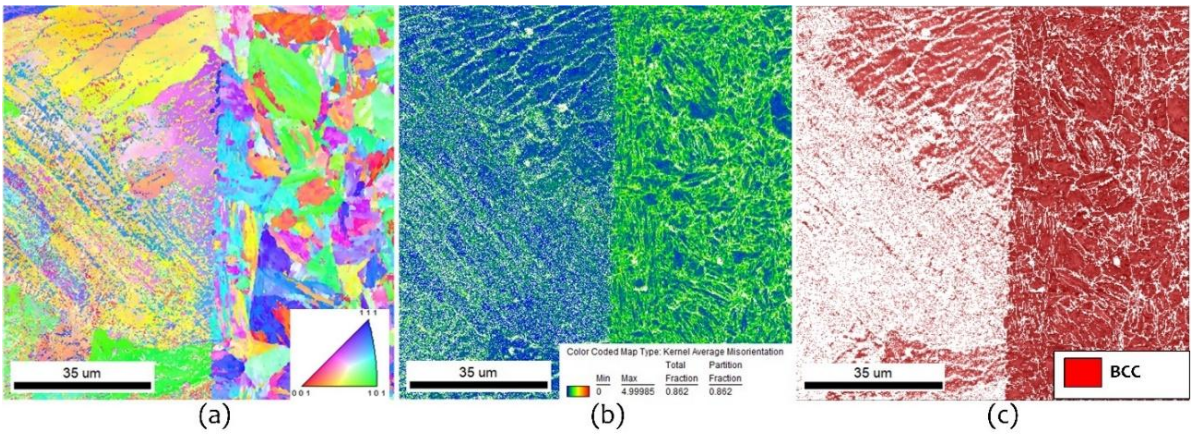


Figure 6.5 : EBSD scan at P91 weld interface (a) IPF map (b) KAM map (d) phase map

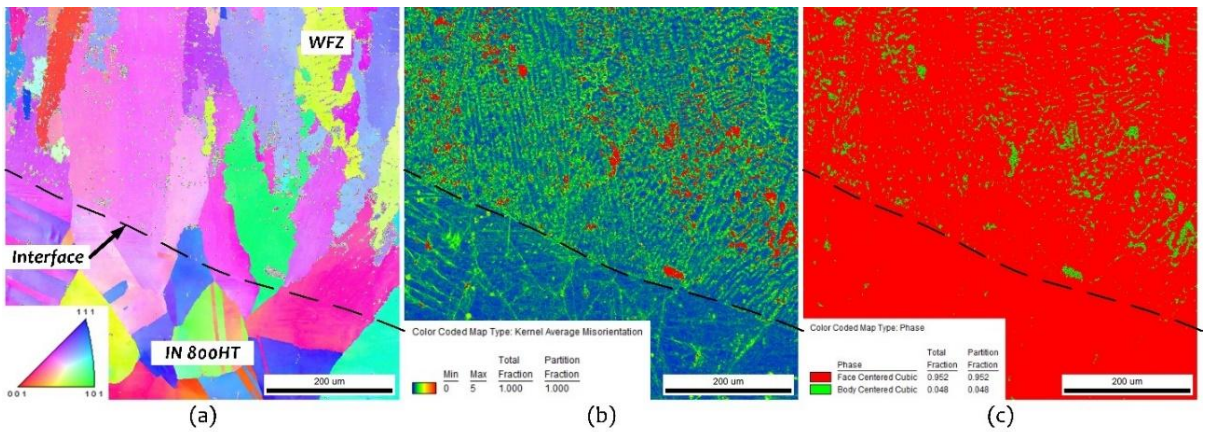


Figure 6.6 : EBSD scan at Incoloy 800HT weld interface (a) IPF map (b) KAM map (c) phase map

6.3 TENSILE PROPERTIES

The study examined the tensile strength of the welded joint in both AW and PWHT states (Figure 6.7). The tensile test results are summarized in Table 6.2. The AW and PWHT state standard specimens had ultimate tensile strengths (UTS) of 546 MPa and 576 MPa, respectively, and their yield strengths (YS) were 171 MPa and 123 MPa, respectively. The AW standard specimen failed from the Incoloy 800HT base metal side, while the PWHT standard specimen failed from the WFZ. The stress-strain curves are depicted in Figure 6.7. The KAM map exhibited a significant strain distribution in the heat affected zone (HAZ) of the P91 material. Consequently, it can be inferred that the failure originated from the region of the P91 HAZ. However, it is essential to note that the tensile strength of a material is influenced by various factors related to its microstructure, such as grain size, grain shape, grain boundary orientation, and other pertinent characteristics. The presence of segregated elements at the SGBs can lead to a notable degradation in mechanical strength.

In some cases, high KAM values can lead to improved tensile strength due to the presence of substructures, such as secondary phase particles, that reinforce the material and enhance its mechanical properties. In support of such exceptional behavior, few works of literature have reported that in Ni-based superalloys, failure occurred from the region where the high-stress concentration was observed in the EBSD KAM map (H. Zhang et al., 2021; Zhou et al., 2020).

Further, a fractography study was conducted to confirm the mode of fracture. Figure 6.8(a-d) shows the fractured surface micrographs of standard AW, standard PWHT, subsize AW, and subsize PWHT specimens, respectively. Figure 6.8(a) shows tear ridges and macro dimples, suggesting a mixed failure mode in the AW standard tensile specimen. The macro voids were present as microvoids must have combined and started the nucleation of the fracture. Figure 6.8(b) confirms the ductile failure mode in the PWHT standard tensile specimen, as dimples were present in the majority, and inclusions were also spotted, which could be the gamma prime phase at the grain boundary. The AW subsize tensile specimen (Figure 6.8(c)) had a mixed failure mode with cleavage facets along the dimples. The significant presence of cleavage facets hints that fracture propagated along this path, possibly the IN 800HT weld interface. The PWHT subsize tensile specimen fractured surface in Figure 6.8(d) was witnessed with dimples and cleavage facets confirming the ductile nature of the WFZ and mixed mode of failure.

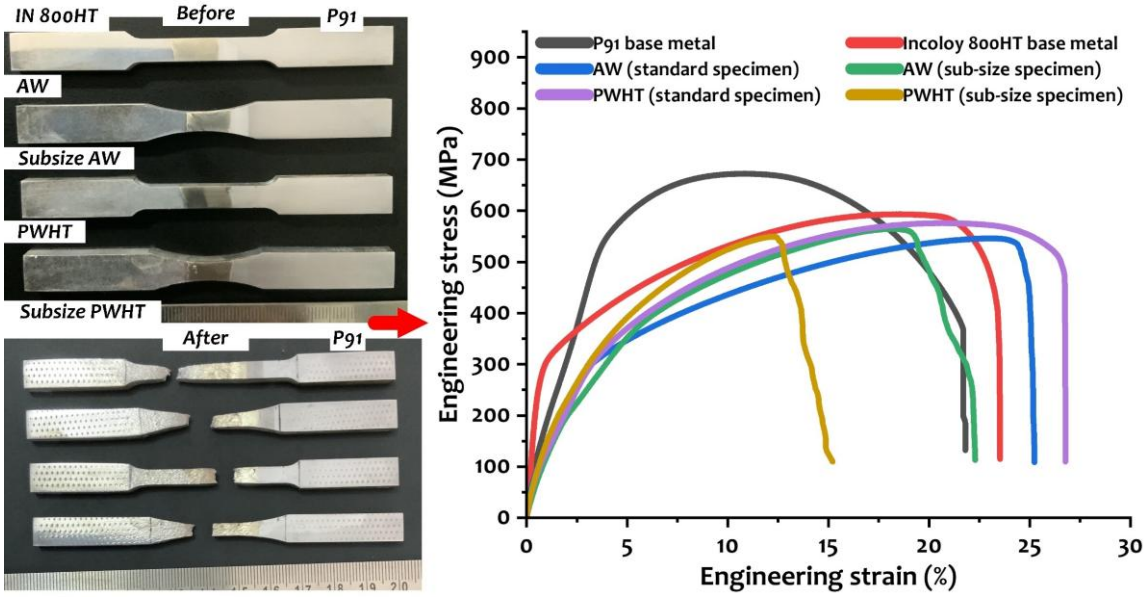


Figure 6.7 : Prepared tensile specimens and fractured tensile specimens after testing, with engineering stress-strain curves of base metals and tested tensile specimens

Table 6.2 : Tensile properties of different weld specimens

Specimens	*UTS (MPa)*	*YS [offset 0.2%] (MPa)*	*Elongation (%)*	*Reduction in the area (%)*	*Failure site*
AW (Standard specimen)	546 ± 5	197 ± 5	33 ± 2	52 ± 2	Base metal Incoloy 800HT
AW (Subsize specimen)	561 ± 5	-	15 ± 2	11 ± 3	Incoloy 800HT weld interface
PWHT (Standard specimen)	576 ± 5	182 ± 6	27 ± 2	44 ± 3	WFZ
PWHT (Subsize specimen)	540 ± 5	-	20 ± 3	12 ± 3	WFZ

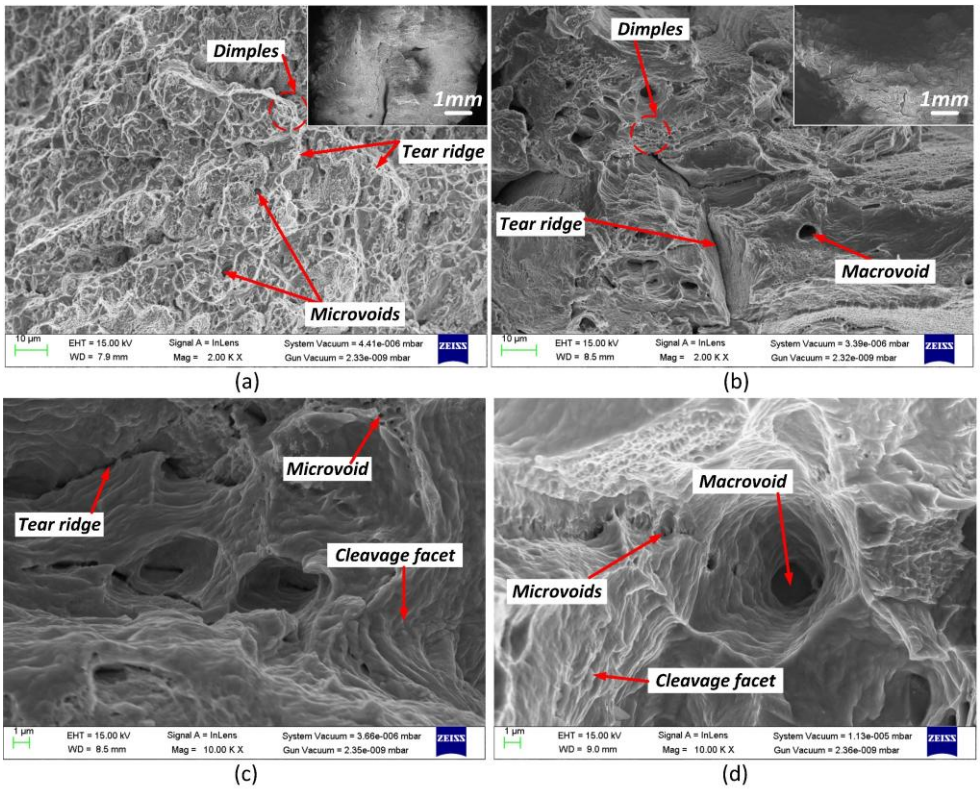


Figure 6.8 : Fractography SEM micrographs of (a) AW state standard tensile specimen (b) PWHT state standard tensile specimen (c) AW state subsize tensile specimen (d) PWHT state subsize tensile specimen

6.4 MICROHARDNESS PROPERTIES

The Vickers microhardness tests were conducted on etched metallographic specimens, as shown in Figure 6.9. The microhardness variation in a weld has been depicted using 2D contour plots created in OriginPro 2022b software. Figure 6.9 depicts the microhardness variation along and across the weld in the as-welded (AW) state, with the highest values in the CGHAZ region (582 HV) near the weld center. The values decrease gradually from the CGHAZ to ICHAZ and match the base metal readings. The increase in microhardness in the FGHAZ (342 HV) and CGHAZ regions is attributed to the dissolution of precipitates. The ICHAZ had a minimum value of 199 HV. The WFZ has a uniform distribution with an average of 256 ± 15 HV. The Incoloy 800HT HAZ in the AW state has an average microhardness of 243 ± 15 HV, and the base metal regions have an average of 238 ± 15 HV and 253 ± 15 HV for Incoloy 800HT and P91, respectively. The contour profile across

the weld shows a rise in microhardness in the P91 HAZ region and remains constant along the remaining region.

The 2D contour map of microhardness in the PWHT specimen is shown in Figure 6.9. PWHT is known to temper the microstructure, re-evolve dissolved precipitates, and improve toughness (Kumar and Pandey, 2022). The CGHAZ region was found to have a drastic reduction in microhardness to 268 ± 15 HV. The CGHAZ region above the weld center and near the top weld region was observed with a peak microhardness of 441 HV. The FGHAZ region also dropped to an average microhardness of 257 ± 20 HV. The ICHAZ region showed an increase in microhardness levels, with an average of 221 ± 10 HV. The resurfacing of carbide precipitates homogenized the P91 HAZ microhardness during tempering. In addition to the changes observed P91 HAZ region, the WFZ after PWHT also suffered a decline in microhardness. An average microhardness of 262 ± 15 HV was measured in the WFZ. The Incoloy 800HT HAZ and the base metal region also showed a drop in average microhardness to 235 ± 20 HV and 224 ± 15 HV, respectively. The reduction in microhardness can likely be attributed to the precipitation of the Cr-rich $M_{23}C_6$ phase, which occurs at the PWHT temperature of 760 °C. The microhardness at the P91 weld interface was 268 HV in the top weld region and 266 HV near the weld root region. While there was no significant variation along the Incoloy 800HT weld interface, the microhardness at the Incoloy 800HT weld interface in the PWHT state was 212 ± 5 HV.

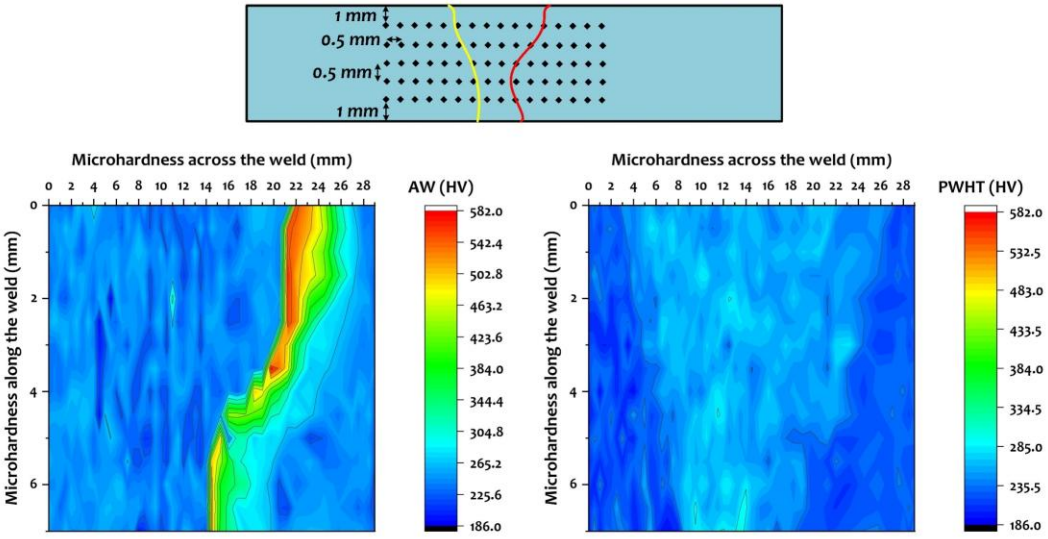


Figure 6.9 : 2D contour profile plot of microhardness across the specimen in AW and PWHT state

6.5 CHARPY IMPACT TOUGHNESS

The study conducted V-notched Charpy impact toughness tests on AW and PWHT specimens, as shown in Figure 6.10. The impact tests were conducted as per ASTM E23 (ASTM E 23-12c, 2012). The AW specimen had an average Charpy impact toughness value of 82 J and exhibited a ductile mode of failure with shear lips and lateral expansion of 2.5 mm. The PWHT specimen had a slightly lower average Charpy impact toughness value of 64 J. The slight increase in toughness in the PWHT specimen could be attributed to carbide precipitation in the WFZ which helped to stabilize the grain boundaries and dislocations. Both specimens had lower Charpy impact toughness compared to the base metal toughness of P91 (102 J) and Incoloy 800HT (110 J). The Charpy impact toughness of the weld met the set standards. The fractography micrographs (Figure 6.10(a-b) showed a uniform distribution of dimples and cleavage facets, indicating a hybrid mode of failure that was predominantly ductile. The low Charpy impact toughness may have been caused by the formation of fusion centerline and columnar dendrites, which provide an easy path for fracture propagation. A reported study also suggests that the precipitation of $M_{23}C_6$ carbides can improve the mechanical properties of Ni-based alloys (Sims et al., 1987).

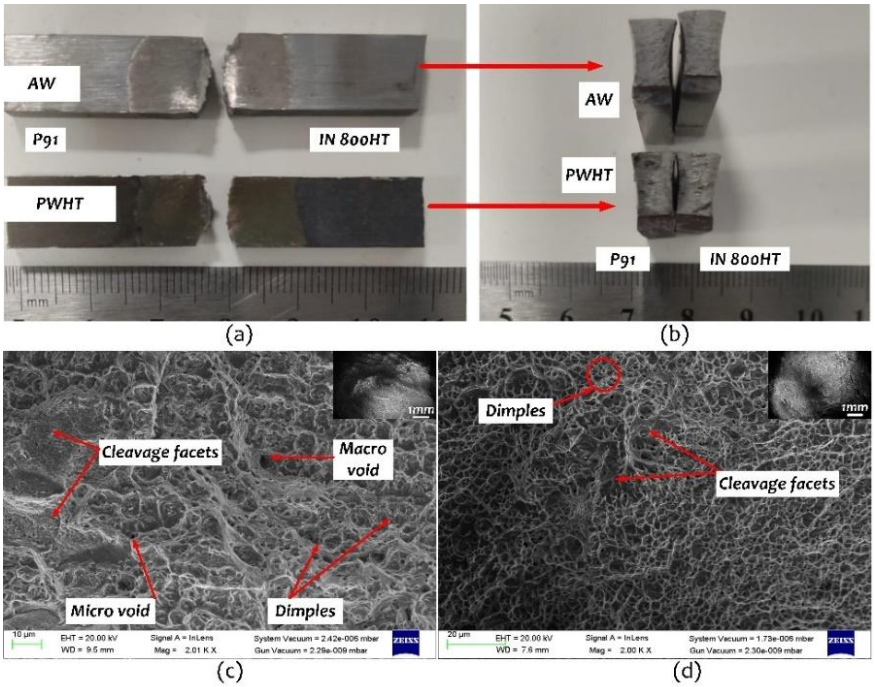


Figure 6.10 : V-notched Charpy impact toughness specimens (a) after fracture (b) fractured tips

...